Journal of Network Intelligence
Taiwan Ubiquitous Information
 ISSN 2414-8105
Volume **9**, Number **4**, November **2024**

Suppression Strategy of Sub-synchronous Oscillation in OWF Connected to the Grid Through MMC-HVDC

Ren-Wu Yan*, Fu-Wei Fu, Yun-Zhang Liu

College of Electronic Electrical and Physics
Engineering Research Center for Smart Grid Simulation Analysis and Integrated Control
Fujian University of Technology, Fuzhou 350118, China
16370379@qq.com, 834981817@qq.com, 745744110@qq.com

Ning Yu

Department of Computing Sciences
State University of New York Brockport College, NY 14420, USA
nyu@brockport.edu

Zhi-Hong Zhang

College of Electronic Electrical and Physics
Engineering Research Center for Smart Grid Simulation Analysis and Integrated Control
Fujian University of Technology, Fuzhou 350118, China
1303220922@qq.com

*Corresponding author: Ren-wu Yan

Received May 18, 2023, revised September 11, 2023, accepted January 9, 2024.

Abstract. *Currently, modular multilevel converter-based flexible direct current transmission technology (MMC-HVDC) is the prevalent method for connecting long-distance offshore wind farms (OWF) to large power grid systems. Due to unique meteorological conditions at sea and the utilization of substantial wind turbines, offshore doubly-fed wind turbines possess a higher axial elastic coefficient compared to their onshore counterparts. When linked to the grid via MMC-HVDC, two types of sub-synchronous oscillations occur: natural torsional vibrations within the wind turbine shafting and sub-synchronous oscillations resulting from interactions between the wind turbine and devices in the MMC-HVDC converter control system. To address these issues, a MMC-HVDC grid connection model for offshore long-distance doubly-fed wind farms has been developed. A cloud computing platform-based wind farm data acquisition system is employed for remote wind turbine data collection. Eigenvalue analysis and participation factors are utilized to determine oscillation modes and corresponding strongly correlated state variables arising from interactions between wind turbine shaft torsional vibration and converter devices. Upon identifying the correlations of state variables, a suppression strategy involving a circulating current suppression DC control collaborative virtual resistance controller is proposed to mitigate sub-synchronous oscillations. The efficacy of the suggested suppression approach is validated using PSCAD/EMTDC electromagnetic transient simulation software.*

Keywords: Cloud computing, Flexible DC power transmission, Offshore wind farm, Mode analysis

1. **Introduction.** With the development of modern power systems, the application of wind power as a clean energy source is becoming increasingly widespread, among which offshore wind power is particularly unique among all wind power generation methods due to its abundant wind resources. Most offshore wind turbines use single machine large capacity generators, which have longer blades and larger inertia coefficients compared to onshore wind turbines. The sub-synchronous oscillation phenomenon generated by offshore doubly fed wind turbines using full power inverters when connected to the onshore power grid through flexible DC transmission systems is also different from that generated by onshore wind turbines.

It is of great significance to analyze the sub-synchronous oscillation caused by the grid connection of wind farms via MMC-HVDC (Modular Multilevel Converter based High Voltage Direct Current) and its suppression measures. In Reference [1], the author built a grid connected small-signal modeling for the wind farm connected to the flexible and straight system at the weak sending end, studied the dominant mode of sub-synchronous oscillation in different physical scenarios at different time scales, and revealed the impact of control loop bandwidth on oscillation by analyzing participation factors. In addition to the methods for analyzing the phenomenon of sub-synchronous oscillation mentioned above, the participation factor method was introduced in Reference [2], which was used to deduce the dominant mode and key parameters causing system oscillation after the grid connection of a doubly fed wind farm. The influence of the parameters of the commutation suppression controller on the stability of the grid connection system was also analyzed. The author of Reference [3] used eigenvalue analysis to obtain two types of sub-synchronous oscillations generated by offshore wind farms connected to the VSC-HVDC grid. Based on this, the relevant variables of two different vibration modes were studied, and an additional damping controller was designed to suppress sub-synchronous oscillations. Reference [4] analyzed the impact of reduced AC power grid strength on the stability of MMC-HVDC system by establishing an equivalent impedance model of AC power grid, proposed a method for identifying the equivalent impedance of reactive power injection into the power grid, and verified the accuracy of the identification method.

1.1. **Related work.** The integration of wind power generation into the DC transmission system is accompanied by changes in the development of DC transmission at different stages, especially in the study of sub-synchronous oscillations caused by wind power external high-voltage DC transmission. Divide the DC transmission system into VSC-HVDC stage and MMC-HVDC stage. Firstly, in the first stage, the wind farm is connected to the grid through VSC-HVDC, and a large amount of research has been conducted on the problem of sub-synchronous oscillation of wind turbines connected to flexible DC transmission. Based on the system equivalent model, Reference [5] analyzed the impact of oscillation from factors such as the number of connected wind farms, wind speed, and load. By determining the sensitivity index of state variables to impedance, the influence of various control parameters on the system equivalent impedance was analyzed. In Reference [6], the author studied the sub-synchronous oscillation caused by a direct drive fan through flexible DC transmission, obtained the oscillation mode using eigenvalue analysis, and studied the impact of fan aggregation characteristics on system stability. In the second stage of grid connection through the MMC-HVDC system, Reference [7] analyzed the high-frequency phenomenon and generation mechanism in engineering systems, analyzed the impact of high-frequency on various components in the DC system, and proposed a two-stage inverse time submodule protection strategy. Reference [8] establishes a transient synchronous stability model for the PLL-GSC (Phase Locked Loop Grid Structural Converters) type MMC-HVDC grid connected system. The phase diagram curve

analysis method is used to analyze the impact of converter instability mechanism on the dynamic changes of grid current after grid faults, and measures are proposed to regulate the transient synchronous stability of active current stability systems using dynamic systems. Reference [9] found that the transmission capacity of flexible and straight systems is constrained by power electronic devices, and proposed a modulation strategy based on third harmonic injection, which affects the operation of MMC-HVDC systems.

1.2. **Motivation and contribution.** To address the deficiencies of the offshore wind turbine external DC system's grid-connected sub-synchronous oscillation suppression issue, this article conducts research on the phenomenon of sub-synchronous oscillation caused by offshore wind farms connected to the MMC-HVDC system. Some of the main contributions of this article are as follows:

- The next synchronous oscillation analysis method is selected from the simplified mathematical model, and the equivalent method of linearization of nonlinear system based on small disturbance method is presented.
- By analyzing the sub-synchronous oscillation types, the optimized suppression strategy is proposed.

1.3. **Layout of the paper.** The following is the rest of the paper's layout: a simulation model of offshore wind farms connected to the MMC-HVDC system is constructed in Section 2. The mechanism of sub-synchronous oscillation caused by offshore wind farms connected to the MMC-HVDC system is analyzed in Section 3. Section 4: Proposing a collaborative virtual resistance suppression strategy based on CCSC controller. The mechanism analysis of sub-synchronous oscillation and the effectiveness of suppression measures are verified by simulation in Section 5. Finally, we will discuss the conclusion.

2. DFIG based on cloud platform data collection system connected to the grid through MMC-HVDC model.

2.1. **Cloud platform data collection system.** SCADA system diagram of wind farm cloud computing platform is shown in Figure 1. The real-time data of the wind farm and DC system is sent to the dispatch center through their respective intelligent terminals. The dispatch center uploads the collected data to the cloud computing platform through the internet, and the cloud computing platform analyzes whether there is a risk of sub-synchronous oscillation in the system based on the real-time data [10]. If the calculation results indicate a risk of sub-synchronous oscillation in the system, the calculation results will be fed back to the dispatch center by the cloud computing platform, and controller parameter modification instructions will be issued to the intelligent terminals of the wind farm and DC system based on the feedback.

2.2. **DFIG connected to the grid through MMC-HVDC model.** DFIG grid connected system structure through MMC-HVDC is shown in Figure 2. The offshore wind farm uses a flexible DC transmission system to transmit electrical energy to the load center over long distances, further improving its absorption capacity. The offshore wind farm in this article is mainly composed of doubly fed wind turbines, which are mainly connected by GSC, DFIG motors, and RSC through DC bus capacitors. Due to the large capacity of DC bus capacitors, the voltage fluctuations caused in the generator are relatively small, and can be ignored during modeling [11]. In the grid connected system, the offshore wind farm is connected to an external step-up transformer and further boosted at the gathering busbar to reach the voltage level of the external flexible DC system, and finally connected to the large power grid through the flexible DC transmission system. The MMC-HVDC system in this article consists of a sending end rectifier station, a DC

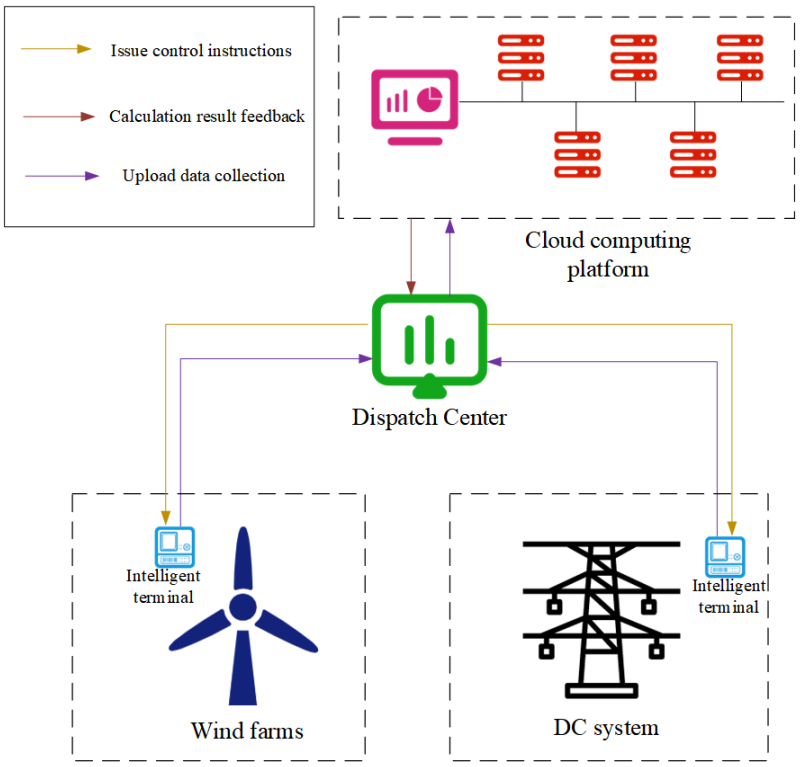

FIGURE 1. SCADA System Diagram of Wind Farm Cloud Computing Platform

line, and a receiving end inverter station. The sending end rectifier station and the receiving end inverter station have the same mathematical model, so only one end of the sending end rectifier station and the receiving end inverter station can be considered in mathematical modeling [12]. The wind farm is equivalent to a single doubly fed wind turbine with a capacity of 5MW; The rated capacity on the DC side is 900WM; DC voltage level ±230kV.

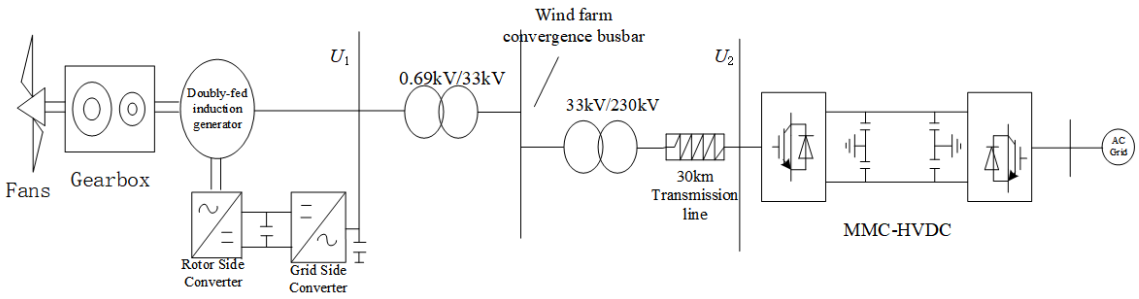

FIGURE 2. DFIG Grid Connected System Structure Through MMC-HVDC

2.3. **Mathematical Model of Doubly Fed Wind Turbine and MMC-HVDC Grid Connection System.** This section provides an in-depth analysis of the doubly fed wind turbines, converters, and wind turbine shaft systems in wind farms, establishing a wind power system model, laying the foundation for subsequent analysis of sub synchronous oscillations caused by MMC-HVDC grid connection in wind farms. In the actual analysis of sub-synchronous oscillation mechanisms, establishing a detailed mathematical model

can accurately analyze their oscillation mechanism. However, the detailed mathematical model of wind turbines is a complex system of multivariable differential equations, and the solving process is extremely complex. Therefore, the wind turbine is divided into three blocks for modeling. The first block is a wind turbine model, the second block is a generator model, and the third block is a control model for the turbine and grid side converter.

Firstly, model the transmission model of the wind turbine. This includes a wind turbine.

2.4. **Aerodynamic model of wind turbine.** Wind turbines are an important power device that can convert wind energy into mechanical energy to drive equipment such as electric motors or generators. The wind turbine is the unit that converts the kinetic energy of air into mechanical energy in a fan. According to Bates theory, C_p is calculated using the fitting curve method.

The power coefficient C_p is about λ and β. The nonlinear expression of is as follows.

$$\begin{cases} \omega_h = \dfrac{\omega_m}{GR} \\ \lambda = \dfrac{2.237 v_w}{\omega_h} \\ C_p = \dfrac{1}{2}\left(\lambda - 0.022\beta^2 - 5.6\right) e^{-0.17\lambda} \end{cases} \tag{1}$$

In the above equation, v_w represents the wind speed, λ is the tip speed ratio, β is the blade torque angle, C_p is the power coefficient, and T is the torque, ω_h is the mechanical speed of the turbine, ω_h is the hub speed, and GR is the gear ratio. When the pitch angle is a constant value, the wind power generation efficiency value C_p value caused by the change in blade tip speed ratio also changes. That is to say, there is a one-to-one relationship between the two, and there is only one connection, which is the variation rule of the maximum wind power generation conversion efficiency value. The input setting for the wind energy utilization coefficient in this article is a fixed value of 0.29.

2.5. **Doubly fed generator model.** To simplify the analysis, the generator can follow the three-phase symmetry of the winding and the sinusoidal distribution of the air gap rotating magnetic flux, ignoring eddy current losses, magnetic saturation, and generator excitation. Transform the three-phase stationary coordinate system to the dq two-phase rotating coordinate system, and achieve the coordinate transformation through $C_{3/2}$ and C_{VR} as follows:

$$\begin{cases} C_{3/2} = 2/3 \begin{bmatrix} 1 & -1/2 & -1/2 \\ 0 & \sqrt{3}/2 & -\sqrt{3}/2 \end{bmatrix} \\ C_{VR} = \begin{bmatrix} \cos\theta & \sin\theta \\ -\sin\theta & \cos\theta \end{bmatrix} \end{cases} \tag{2}$$

In the above equation: θ The angle between the horizontal axis of the two-phase stationary coordinate and the two-phase rotating coordinate. Use the subscripts to represent the d-axis and q-axis of the two-phase rotation coordinates, as well as the stator and rotor voltage equations of the generator. The generator model obtained from the above conditions is as follows:

Voltage equation:

$$\begin{cases} u_{ds} = R_s i_{ds} - \omega_1 \psi_{qs} + \frac{d}{dt}\psi_{cs} \\ u_{qs} = R_s i_{qs} + \omega_1 \psi_{ds} + \frac{d}{dt}\psi_{qs} \\ u_{dr} = R_r i_{dr} - s\omega_s \psi_{qr} + \frac{d}{dt}\psi_{dr} \\ u_{qr} = R_r i_{qr} + s\omega_s \psi_{dr} + \frac{d}{dt}\psi_{qr} \end{cases} \tag{3}$$

Magnetic linkage equation:

$$\begin{cases} \psi_{ds} = L_{ss} i_{ds} + L_m i_{dr} \\ \psi_{qs} = L_{ss} i_{qs} + L_m i_{qr} \\ \psi_{dr} = L_m i_{ds} + L_{rr} i_{dr} \\ \psi_{qr} = L_m i_{qs} + L_{rr} i_{qr} \end{cases} \tag{4}$$

In the above equation: ω_s represents the rotational angular velocity of the dq coordinate system, is the rotational angular velocity of the stator magnetic field, and s represents the generator slip; u, i, and ψ respectively represent the voltage, current, and magnetic flux of each winding stator and rotor; R_s, R_r, L_{ls}, and L_{lr} represent the resistance and leakage inductance of the stator and rotor, respectively. L_m represents mutual inductance, and $L_{ss} = L_m + L_{ls}$ represents the stator self inductance. Similarly, L_{rr} represents the rotor side. Furthermore, we can obtain the calculation formula for electromagnetic torque as follows $T_e = L_m(i_{qs} i_{dr} - i_{ds} i_{qr}) = \psi_{ds} i_{qs} - \psi_{qs} i_{ds}$

2.6. **DFIG machine side and grid side converter control model.** The machine side frequency converter adopts generator stator flux decoupling control, which decouples the active and reactive power output of the DFIG stator. Here, power and voltage decoupling is used.

$$\begin{cases} \Delta x_1 = P_{ref} - P_s \\ i_{q\cdot r.ref} = K_{p1}\left(P_{ref} - P_s\right) + K_{i1} x_1 \\ \Delta x_2 = i_{q\cdot r\cdot ref} - i_{q.r} \\ u_{q.r} = K_{p2} \cdot \Delta x_2 + K_{i2} x_2 - s_r \omega_s L_m i_{d.s} - s_r \omega_s L_{rr} i_{d.r} \end{cases} \tag{5}$$

$$\begin{cases} \Delta x_3 = u_{ref} - u_s \\ i_{d,r.ref} = K_{p3}\left(u_{ref} - u_s\right) + K_{i3} x_3 \\ \Delta x_4 = i_{d.r.ref} - i_{d.r} \\ u_{d.r} = K_{p4} \cdot \Delta x_4 + K_{i4} x_4 - s_r \omega_s L_m i_{q.s} - s_r \omega_s L_{rr} i_{q.r} \end{cases} \tag{6}$$

In the above equation, P_s and P_{ref} are the reference values for the active power and active power of the machine side stator; s_r is the rotor slip; $i_{d.s}$ and $i_{q.s}$ are the components of the stator current on the d and q axes,respectively; $i_{d.r}$ and $i_{q.r}$ are the components of the rotor current on the d and q axes, respectively. x_λ control variable for rotor side converter, $K_{p\lambda}$ and $K_{i\lambda}$ The proportional coefficient and integral coefficient of the state variable, respectively, $\lambda = 1, 2, 3, 4$. The subscript ref above represents the reference value of the control parameters on the corresponding component.

The grid side converter decouples the voltage in the grid and the power between the grids to obtain:

$$\begin{cases} \Delta x_5 = u_{DC.ref} - u_{DC} \\ i_{\mathrm{d.gref}} = -K_{p5}\left(u_{DC\ \mathrm{ref}} - u_{DC}\right) + K_{i5} x_5 \\ \Delta x_6 = i_{\mathrm{d.g.ref}} - i_{d.g} \\ u_{d.g} = K_{p6} \cdot \Delta x_6 + K_{i4} x_4 + K_{i6} x_6 + X_{Tg} i_{q.g} \end{cases} \tag{7}$$

$$\begin{cases} \Delta x_7 = i_{\mathrm{q.g.ref}} - i_{q.g} \\ u_{q.g} = K_{p7} \cdot \Delta x_7 + K_{i7} x_7 - X_{Tg} i_{d.g} \end{cases} \tag{8}$$

In the above equation, $i_{d.g}$ and $i_{q.g}$ are the components of the grid measurement converter on the d and q axes, respectively; x_λ Control variable for network measurement converter, $K_{p\lambda}$ with $K_{i\lambda}$ The proportional coefficient and integral coefficient of the state variable, respectively, $\lambda = 5, 6, 7$; Voltage at both ends in u_{DC}; X_{Tg} is the reactance between the grid side converter and adjacent transformers in the system.

2.7. **MMC-HVDC mathematical model.** Due to the consistent structure of the converter stations on both sides of the MMC-HVDC system, only one side was discussed during modeling. The π-type equivalent circuit is used for the DC transmission line to obtain the mathematical model of the DC transmission system in the abc three-phase stationary coordinate system:

$$\begin{cases} L_d \frac{dI_{abc}}{dt} = -R_d I_{abc} + (U_{sbx} - U_{abc}) \\ C \frac{dU_{dc1}}{dt} = K_1 \left[\cos(\omega_1 t + \delta_1) i_{a1} + \cos\left(\omega_1 t + \delta_1 - \frac{2}{3}\pi\right) i_{b1} + \cos\left(\omega_1 t + \delta_1 + \frac{2}{3}\pi\right) i_{c1} \right] - i_{cc} \\ C \frac{dU_{dc2}}{dt} = K_2 \left[\cos(\omega_2 t + \delta_2) i_{a2} + \cos\left(\omega_2 t + \delta_2 - \frac{2}{3}\pi\right) i_{b2} + \cos\left(\omega_2 t + \delta_2 + \frac{2}{3}\pi\right) i_{c2} \right] + i_{ck} \\ L_d \frac{di_{dc}}{dt} = U_{d1} - U_{d2} - R_d i_{cc} \end{cases} \tag{9}$$

Due to the difficulty in solving time-varying differential equations, it is obtained through pack transformation into dq synchronous rotating coordinate system:

$$\begin{cases} L_\eta \frac{dI_{d\eta}}{dt} = -R_\eta i_{d\eta} - \omega_\eta L_\eta i_{q\eta} + u_{sd\cdot\eta} - K_\eta U_{dc\cdot\eta} \cos\delta_\eta \\ L_\eta \frac{dI_q}{dt} = \omega_\eta L_\eta i_{d\eta} - R_\eta i_{q\eta} - K_\eta U_{dc\cdot\eta} \cos\delta_\eta \\ C \frac{dU_{dc1}}{dt} = \frac{3}{2} K_1 \left[i_{d1} \cos\delta_1 + i_{q1} \sin\delta_1 \right] - i_{dc} \\ C \frac{dU_{dc2}}{dt} = \frac{3}{2} K_2 \left[i_{d2} \cos\delta_2 + i_{q2} \sin\delta_2 \right] + i_{dc} \\ L_d \frac{di_{dc}}{dt} = U_{dc1} - U_{dc2} - R_d i_{dc} \end{cases} \tag{10}$$

Superscript in Subscript $\eta = 1, 2$ represents one or two sides of the converter station; C is the capacitance impedance value converted into the DC side capacitor; K is the utilization coefficient of DC voltage; δ the angle between the output voltage of the inverter and the system voltage; ω is the fundamental angular frequency of the communication system; R_d and L_d are equivalent resistance and equivalent inductance; i_{dc} is the direct current flowing through the converter stations on both sides; When the d-axis coincides with the AC side voltage vector, $u_{sq.n}$ omit because it is 0.

3. Analysis of sub-synchronous Oscillation Mechanism of Offshore Doubly Fed Wind Farm Connected to the Grid through MMC-HVDC.

3.1. **Theory of Whole System Linearization Based on Small Interference Method.** Firstly, the prerequisite for system linearization is that the system is subject to small disturbances, which must be sufficiently small, such as system load fluctuations, small voltage drops, etc. Secondly, the dynamic characteristics of power system are composed of a set of nonlinear differential equations and nonlinear algebraic equation, and the specific forms are as follows:

$$\begin{cases} \dot{x} = f(x, u, t) \\ y = g(x, u) \end{cases} \tag{11}$$

Large systems generally have multiple inputs and multiple outputs. For an n-order system, assuming the number of inputs is w and the number of outputs is v, the forms of each variable are as follows:

$$\begin{cases} x = [x_1, x_2, \cdots, x_n]^T \\ u = [u_1, u_2, \cdots, u_w]^T \\ g = [g_1, g_2, \cdots, g_v]^T \end{cases} \tag{12}$$

$$\begin{cases} f = [f_1, f_2, \cdots, f_n]^T \\ y = [y_1, y_2, \cdots, y_v]^T \end{cases} \tag{13}$$

The linearized state space equation is obtained by Taylor expansion of the input and output equations at stable points:

$$\begin{cases} \Delta\dot{x} = A\Delta x + B\Delta u \\ \Delta y = C\Delta x + D\Delta u \end{cases} \tag{14}$$

3.2. **Natural torsional vibration analysis of wind turbines based on modal analysis method.** Based on the mathematical modeling of the system and the linearization of the system using the small disturbance method, the feature matrix of the entire system can be obtained as follows:

$$x = A\Delta x \tag{15}$$

In the above equation: A is the coefficient matrix, Δx is divided into the state variables of DFIG and the state variables of DC system MMC-HVDC;

$\Delta x_{DFIG} = [\Delta\theta_1, \Delta\theta_2, \Delta\theta_3, \Delta\omega_1, \Delta\omega_2, \Delta\omega_3, \Delta x_1, \Delta x_2, \Delta x_3, \Delta x_4, \Delta U_{DC}, \Delta x_5, \Delta x_6, \Delta x_7]^T$

$\Delta x_{MMC-HVDC} = [\Delta x_8, \Delta x_9, \Delta x_{10}, \Delta x_{11}, \Delta x_{12}, \Delta x_{13}, \Delta x_{14}, \Delta x_{15}]^T$

According to $AX = \Delta X$. It is possible to obtain the eigenvalues of $A\lambda$ and eigenvectors $\alpha = \sigma + j\omega$, excluding eigenvalues with real parts greater than or equal to 0, the natural torsional vibration analysis of a fan is based on the assumption that the control variable is 0 and there is no external additional torque to obtain the natural torsional vibration frequency of the fan. Among them, damping ratio ζ calculate the modal frequency f_i as follows:

$$\begin{cases} \xi_i = \frac{-\sigma_i}{\sqrt{\sigma_i^2+\omega_i^2}} \\ f_i = \frac{\omega_i}{2\pi} \end{cases} \tag{16}$$

As shown in Table 1 below, the unit values of the three mass blocks of the DFIG shaft system after conversion are M_1, M_2, and M_3, which are the rotational inertia of the converted blade, gearbox, and generator rotor. K_{12} and K_{23} are the stiffness coefficients of the converted blade gearbox and gearbox generator rotor, respectively. p is the number of pole pairs of the electric machine, and G_B is the gearbox ratio.

Table 1. Shafting Parameters

M_1	M_2	M_3	K_{12}	K_{13}
7.777	0.083	0.292	0.521	9.723

According to the above parameters, under the condition of no external additional torque, the shaft system is in an undamped state, which means ignoring the shaft system

damping. By solving the A_Z eigenvalue, the natural torsional vibration frequency can be obtained as f_{M1}=18.27Hz and f_{M2}=4.01Hz.

When the torque T_m=1.2 is applied, the system generates mutual damping between the three mass blocks due to external torque input. The damping effect between the shaft systems changes the original torsional vibration frequency of the fan. The calculated torsional vibration frequencies aref_{M3}=19.03Hz, f_{M4}=17.39Hz, f_{M5}=4.01Hz. The following table shows the damping parameter values of the shaft system after applying torque:

Table 2. Self Damping and Mutual Damping of Each Mass Block After Torque Application

D_1	D_{12}	D_2	D_{23}	D_3
0.01	1.5	0.01	2.8	0.01

Taking into account the two different torque output situations, it can be concluded that the torque input causes the torsional vibration frequency of the fan to move in two ranges. The torsional vibration frequency is around 4.01Hz, and the dominant factor is the stiffness coefficient in the shaft system; The torsional vibration frequency fluctuates around 17Hz 20Hz, and the dominant factor is the damping coefficient in the shaft system.

3.3. **DFIG grid-connected synchronous oscillation characteristics by MMC-HVDC.** After obtaining the natural Torsional vibration frequency of the fan shaft system from the previous section, calculate the sub-synchronous oscillation mode under the initial state of the system. The proportional control parameters and integral gain parameters of the system are shown in Tables 3 and 4.

Table 3. System Proportional Gain Parameters

k_{p1}	k_{p2}	k_{p3}	k_{p4}	k_{p5}	k_{p6}	k_{p7}
2	1	2	0.65	0.65	0.8	0.8

Table 4. System Integral Gain Parameters

k_{i1}	k_{i2}	k_{i3}	k_{i4}	k_{i5}	k_{i6}	k_{i7}
0.02	0.05	0.02	0.025	0.025	0.01	0.01

The established state space matrix uses modal analysis to solve the eigenvalues and eigenvectors. The system has seven pairs of oscillation modes, and the real part of the eigenvalues of mode numbers 3, 4, and 7 shows values greater than 0, indicating that the system is in a divergent state. The following seven pairs of oscillation modes include sub-synchronous oscillation modes and supersynchronous oscillation modes, resulting in seven pairs of oscillation modes, as shown in Table 5 below.

For the modes obtained from the above analysis, we introduce participation factors to analyze the participation of each state variable in each mode. The formula for calculating the participation factor is as follows

$$P_{ki} = U_{ki}V_{ki} \tag{17}$$

Table 5. System Integral Gain Parameters

Modal Number	Eigenvalue	Frequency	Damping Ratio
$\lambda_{1,2}$	$-38.863 \pm a119.56i$	19.02Hz	0.309
$\lambda_{3,4}$	$23.472 \pm 109.26i$	17.4Hz	-0.21
$\lambda_{5,6}$	$-0.045 \pm 25.217i$	4.01Hz	0.0018
λ_7	$4.06 \times 10^{-18} + 0i$	0	1
$\lambda_{8,9}$	$-9.171 \pm 1.31 \times 10^7 i$	207×10^4Hz	7.05×10^{-7}
$\lambda_{10,11}$	$-8.176 \pm 1.31 \times 10^5 i$	208×10^4Hz	6.24×10^{-5}
$\lambda_{12,13}$	$-0.0001 \pm 0.011i$	1.8×10^{-3}Hz	8.85×10^{-3}

In the above equation, U_{ki} and K_{ki} are eigenvalues λ the left and right eigenvectors of i.

List the participation factors with values greater than 0.1 for each mode.

Table 6. Modal 1,2 Participation Factors

	$\Delta\Psi_{sd}$	$\Delta\Psi_{sq}$	$\Delta\Psi_{rd}$	$\Delta\Psi_{rq}$	Δi_{ds}	Δi_{qs}	Δi_{dr}	Δi_{ds}	x_3	x_4	x_{15}
1,2	0.1451	0.1102	0.1178	0.1091	0.1817	0.5210	0.1763	0.1482	0.2253	0.2746	0.2048

Table 7. Modal 1,2 Participation Factors

	$\Delta\Psi_{rd}$	Δu_{dr}	Δi_{qs}	Δi_{dr}	Δi_{qs}	Δx_2	Δx_3	Δx_4	Δx_5	Δx_{10}
3,4	0.4206	0.5412	0.5546	0.4365	0.7812	0.4833	0.2153	0.1146	0.5840	0.4250

Table 8. Modal 5,6 Participation Factors

	$\Delta\Psi_{rq}$	Δx_6
5,6	0.4222	0.1938

Characteristic value $\lambda_{1,2}$ and $\lambda_{3,4}$ the corresponding oscillation frequencies are relatively close, with 19.02Hz and 17.4Hz respectively, but the influencing factors are slightly different about λ the main influencing factors include stator rotor flux, stator rotor current, and rotor side reactive power decoupling.

About λ the main influencing factors of 3,4 include d-axis rotor flux, d-axis rotor voltage, as well as DFIG machine, grid side DC voltage, power decoupling, and torque changes. The reason for this difference is that the controller parameter settings are unreasonable, causing the original control target reference value to deviate far from the actual value. And in response to negative damping, it is easy to generate induction generator effects, and it is necessary to improve the overall parameters of the system.

Characteristic value $\lambda_{5,6}$ the corresponding oscillation frequency is 4.01Hz, mainly due to the resonance between the generator rotor flux and the grid side capacitor voltage. Due to the connection effect of the capacitor and the characterization of the DC side voltage V_{dc}, the value of the capacitor is too large. For the transmission between the machine and grid sides, the system compensation increases, leading to oscillation. This is due to

the sub-synchronous oscillation phenomenon caused by series compensation in a small range of the system. Other modes also have values with participation factors greater than 0.1, but their impact on the overall system is not significant and analysis may not be conducted.

3.4. **Mechanism of sub-synchronous Oscillation in Offshore Wind Power Grid Connection through MMC-HVDC.** From the above analysis results, it can be seen that the offshore doubly fed wind farm connected to the grid through MMC-HVDC mainly has two oscillation modes: SSTI and SSEI. The system generates a disturbance current with a frequency of f_e after removing small interference faults Δi_r, in the fan, the stator side generates a sub-synchronous current with a frequency of $f_0 - f_e$ which induces a sub-synchronous current of the same frequency $f_0 - f_e$ on the rotor side $\Delta i_{e,z,d}$, $\Delta i_{e,z,q}$ the disturbance current generated by the interaction between, and the PWM grid side converter of DFIG $\Delta i_{e,w,d}$, $\Delta i_{e,w,q}$ due to the machine side variable being the input of the grid side, the machine side variable further affects the grid side variable after being disturbed, and finally generates a sub-synchronous current component with the same synchronous frequency $f_0 - f_e$ at the fan end $\Delta i_{g,d}$ and $\Delta i_{g,q}$ the electromagnetic torque caused by this current component is similar to the natural frequency of the DFIG shaft system, causing torsional vibration of the shaft system, SSTI. Active power fluctuation occurs on the rectification side of MMC-HVDC ΔP_e and Reactive Power Fluctuation ΔQ_e, causing the rectifier control system PWM to generate current $\Delta i_{h,d}$, $\Delta i_{h,q}$. The AC power fluctuation caused by transmission through the power grid, SSEI, results in changes in the electromagnetic torque Te in the wind turbine due to the frequency of the disturbance current being also $f_0 - f_e$. The specific propagation process is shown in Figure 3.

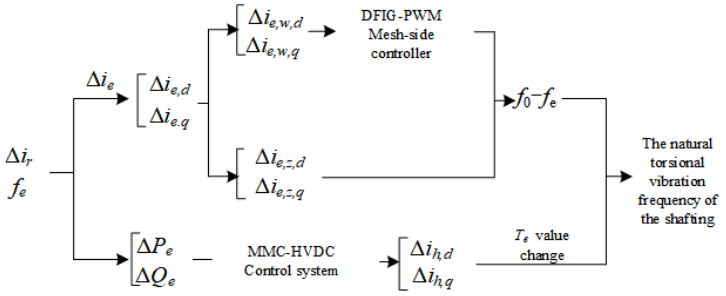

FIGURE 3. Schematic Diagram of Synchronous Oscillation Generation

4. **Collaborative Virtual Resistance Suppression Strategy Based on CCSC Controller in Flexible DC Transmission System.** According to the analysis results above, there are two types of sub-synchronous oscillations in this system. One is caused by the disturbance current, which reacts to the DFIG-PWM network side controller and generates the disturbance current to form SSTI; Another reason is that the disturbance current generates power fluctuations on the control side of the MMC-HVDC system, resulting in the same disturbance frequency as the sub-synchronous frequency, forming SSEI.

The above two different oscillation mechanisms appear in the same model, so the two sub-synchronous oscillations need to be controlled together.

4.1. **Circulation suppression control principle.** The control system of the MMC-HVDC system includes inner loop current control and power outer loop control. In the inner loop current control, the loop suppression control only analyzes the loop current on the bridge arm in the *dq* coordinate and ignores the DC part. In this section, the influence of the DC component will be added to the control strategy based on the original loop suppression strategy. The differential mode expression is:

$$\begin{cases} u_{pj} = \frac{U_{dc}}{2} - u_{diffj} - u_{cirj} \\ u_{nj} = \frac{U_{dc}}{2} + u_{diffj} - u_{cirj} \\ u_{cirj} = L_0 \frac{di_{cirj}}{dt} + R_0 i_{cirj} \end{cases} \tag{18}$$

In the above equation, u_{cirj} is the circulating voltage.

From this, we can obtain the instantaneous expression of MMC-HVDC transmission energy:

$$\frac{dW_j}{dt} = u_{pj} i_{pj} + u_{nj} i_{nj} \tag{19}$$

Bring Equation (18) into Equation (19) to obtain the energy equation represented by the circulating voltage u_{cirj}:

$$\frac{dW_j}{dt} = u_{diffj} i_j + (U_{dc} - 2u_{cijj})\, i_{cijj} \tag{20}$$

The internal circulation is composed of a DC component and a second harmonic component. The second harmonic component is still controlled by the circulation suppression controller, which controls the size of the DC component to suppress the DC power fluctuations generated by the system. Furthermore, the energy changes in the DC system are determined by both AC power and DC power. Therefore, controlling the DC power helps to suppress the sub-synchronous oscillations generated by the DC in the internal current. The direct current component in the circulation is:

$$R_0 i_{cir0} = \frac{U_{dc}}{2} - u_{com0} \tag{21}$$

In the above equation, i_{cir0} represents the zero-axis component of the DC component in the circulation; u_{cir0} represents the zero-axis component of the common mode voltage in the circulating current.

Rewrite Formula (21) as:

$$\frac{i_{cir0}}{\frac{U_{dc}}{2} - u_{\mathrm{com}\ 0}} = \frac{1}{R_0} \tag{22}$$

The circulating current suppressor adopts closed-loop negative feedback control, with the input of the DC component being i_{cir0}, the tracking reference value set to i^*_{cir0} and the initial value of the reference value i^*_{cir0} set to one-third of the actual DC current value at the stable operating point. Figure 4 shows the closed-loop control system for the DC component of internal circulation. The transfer function in the above figure adopts PI control, and the parameters of k_{p8} and k_{i8} are set to 0.8 and 16.

4.2. **Suppression strategy of additional virtual resistance controller for rotor side converter.** From the perspective of the induction generator effect generated by the external MMC-HVDC system, the influence of RSC (Rotor side controller) control parameters on the response characteristics of SSTI is studied. By equating RSC at sub-synchronous oscillation frequency to resistance, an equivalent model of RSC system is established to study the response characteristics of RSC system to SSTI. Based on this, the proportional integration relationship between RSC equivalent resistance and the control

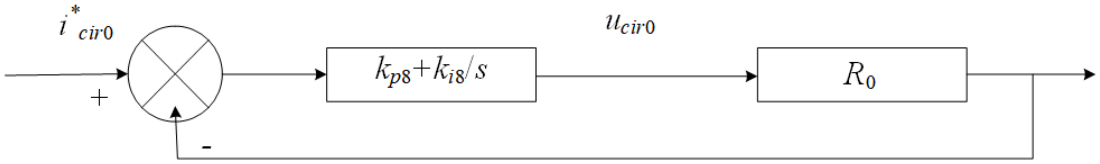

FIGURE 4. Closed Loop Control of Circulating Current DC Component

inner and outer loops is derived, and the parameter settings of virtual resistance controller are determined.

From the relationship between the rotor current and the output voltage of the rotor side converter, it can be concluded that:

$$\begin{cases} u_{dr} = \left(K_{p2} + \frac{K_{i2}}{s}\right)\left[\left(K_{p1} + \frac{K_{i1}}{s}\right)\left(P_s - P_{s\_ref}\right) - i_{dr}\right] \\ u_{qr} = \left(K_{p2} + \frac{K_{i2}}{s}\right)\left[\left(K_{p1} + \frac{K_{i1}}{s}\right)\left(Q_s - Q_{s\_ref}\right) - i_{qr}\right] \end{cases} \tag{23}$$

At the initial moment, the reference value increment is 0,ΔP_{s_ref}=0, ΔQ_{s_ref}=0, rewrite Equation (23) as:

$$\begin{cases} \Delta u_{dr} = \left(K_{p2} + \frac{K_{i2}}{s}\right)\left[\left(K_{p1} + \frac{K_{i1}}{s}\right)\Delta P_s - \Delta i_{dr}\right] \\ \Delta u_{qr} = \left(K_{p2} + \frac{K_{i2}}{s}\right)\left[\left(K_{p1} + \frac{K_{i1}}{s}\right)\Delta Q_s - \Delta i_{qr}\right] \end{cases} \tag{24}$$

In the case of stator voltage orientation, the d-axis coordinate coincides with the stator voltage vecto U_s direction, ignoring the influence of stator resistance. At the same time, the stator flux vector direction is also consistent with the negative direction of the q-axis, and lags behind the stator voltage by 90° in the direction. The expression of stator current and power can be obtained from the relationship between stator voltage, magnetic flux, and current:

$$\begin{cases} i_{ds} \approx -\frac{L_m}{L_s} i_{dr} \\ i_{qs} \approx -\frac{U_s}{\omega_s L_s} - \frac{L_m}{L_s} i_{qr} \end{cases} \tag{25}$$

$$\begin{cases} P_s = u_{ds} i_{ds} = -\frac{U_s L_m}{L_s} i_{dr} \\ Q_s = u_{ds} i_{qs} = -\frac{U_s^2}{\omega_s L_s} - \frac{U_s L_m}{L_s} i_{qr} \end{cases} \tag{26}$$

In the above equation: L_m is the equivalent mutual inductance of the stator and rotor windings in the dq coordinate system; L_s is the equivalent self inductance of the stator in the dq coordinate system; ω_s is the rotational angular velocity of the synchronous magnetic field. Derive Equation (26) to obtain the power increment equation:

$$\begin{cases} \Delta P_s = -\frac{L_m}{L_s} U_s \Delta i_{dr} \\ \Delta Q_s = -\frac{L_m}{L_s} U_s \Delta i_{qr} \end{cases} \tag{27}$$

$$\begin{cases} \Delta u_{dr} = \left(K_{p2} + \frac{K_{i2}}{s}\right)\left[-\left(K_{p1} + \frac{K_{i1}}{s}\right) U_s L_m / L_s - 1\right] \Delta i_{dr} \\ \Delta u_{qr} = \left(K_{p2} + \frac{K_{i2}}{s}\right)\left[-\left(K_{p1} + \frac{K_{i1}}{s}\right) U_s L_m / L_s - 1\right] \Delta i_{qr} \end{cases} \tag{28}$$

Add the two phase components of the d and q axes in Equation (28) to obtain the relationship between the rotor current increment and the output voltage of the rotor converter:

$$\begin{aligned}\Delta u_r &= \left[\frac{K_{i2}}{\omega^2}\left(K_{i1}U_sL_m/L_s\right) - K_{p2}\left(1 + K_{p1}U_sL_m/L_s\right)\right]\Delta i_r \\ &= \left[\left(\frac{K_{i2}K_{i1}}{\omega^2} - K_{p2}K_{p1}\right)U_sL_m/L_s - K_{p2}\right]\Delta i_r\end{aligned} \tag{29}$$

In the above equation: ω is the angular frequency of SSTI. When there is disturbance current in the rotor current Δi_r, the front of the disturbance current is equivalent to a rotor resistance R_{RSC}, and the relationship between the equivalent resistance R_{RSC} and the proportional coefficient is as follows:

$$R_{RSC} = \frac{\Delta u_r}{-\Delta i_r} = \left[K_{p2} - \left(\frac{K_{i2}K_{i1}}{\omega^2} - K_{p2}K_{p1}\right)U_sL_m/L_s\right] \tag{30}$$

The equivalent resistance R_{RSC} is represented in the DFIG output system to obtain the equivalent circuit diagram of the output system, as shown in Figure 5.

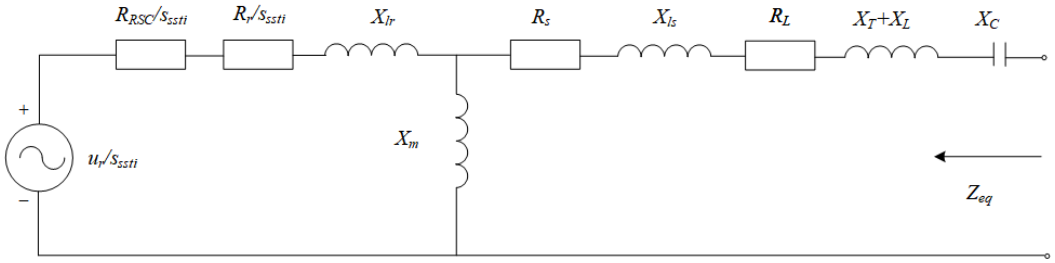

FIGURE 5. Equivalent Circuit of DFIG Wind Power Transmission System

$s_{ssti} = (f_{mi} - f_0)/f_{mi}$ is the slip of the SSTI frequency, where f_{mi} is the compensated system SSTI oscillation frequency $f_{mi} = f_0\sqrt{X_c/\sum X}$, f_0 is the power frequency 50Hz, X_C is the compensation capacitance, and $\sum X$ is the equivalent total reactance of the system. Due to $f_{mi} < f_0$, $s_{ssti} < 0$. At SSTI frequency, u_r/s_{ssti} is the equivalent rotor voltage, R_{RSC}/s_{ssti} is the RSC equivalent resistance, and R_r/s_{ssti} is the rotor winding equivalent resistance. Therefore, the equivalent resistance of the rotor in the system at SSTI frequency is negative, and $R_r/s_{ssti} + R_{RSC}/s_{ssti} < 0$ [20]. X_{lr} and X_{ls} represent the rotor leakage reactance and stator leakage reactance, respectively, while X_L, X_T, R_S, R_L represent the reactance and resistance of the line and transformer; X_m represents mutual inductance. When the line inductance is ignored, $R_{eq} = R_{RSC}/s_{ssti} + R_r/s_{ssti} + R_s + R_L$. When $R_{eq} < 0$, the system exhibits negative resistance characteristics, that is, when the system is disturbed by sub-synchronous frequency, sub-synchronous oscillation phenomenon will occur.

4.3. **Using Virtual Resistance Controller to Suppress SSTI.** Sub-synchronous frequencies, the equivalent resistance of the rotor controller exhibits a negative resistance characteristic to the outside, resulting in a negative system resistance at sub-synchronous frequencies. In order to increase the damping of the system, a virtual resistance controller can be used to change the damping of the system. By adjusting the proportion of the virtual resistance, the fault components of the system can be consumed, thereby restoring the system to a stable state. When designing the proportional coefficient of virtual resistance, as the virtual resistance analyzed above is explicit, the parameters only need to be set to compensate for the equivalent negative resistance generated by RSC under sub-synchronous oscillation, so that the overall system presents positive damping, thereby achieving the goal of suppressing SSTI.

The virtual resistance controller introduces a proportional link using Equation (30), resulting in the following equation:

$$K = R_{RSC} + R_r = \left[K_{p2} + \left(K_{p2}K_{p1} - \frac{K_{i2}K_{i1}}{\omega^2}\right) U_s L_m / L_s\right] + R_r \tag{31}$$

The fixed system parameters are set to: $U_s = 1$p.u, $L_m = 4.5$p.u, $L_s = 4.5+0.1=4.6$p.u, R_r=0.00607p.u. Substituting parameter settings into Equation (31) yields:

$$K = R_{RSC} + R_r = \left[K_{p2} + 0.98\left(K_{p2}K_{p1} - \frac{K_{i2}K_{i1}}{\omega^2}\right)\right] + 0.00607 \tag{32}$$

As shown in Figure 6, the dq-axis components of the circulating current respectively pass through the filter and enter the proportional phase. The purpose is to adjust the dq-axis components of the rotor current, making the system similar to adding a virtual resistor to change the negative damping state of the original system into a positive damping state.

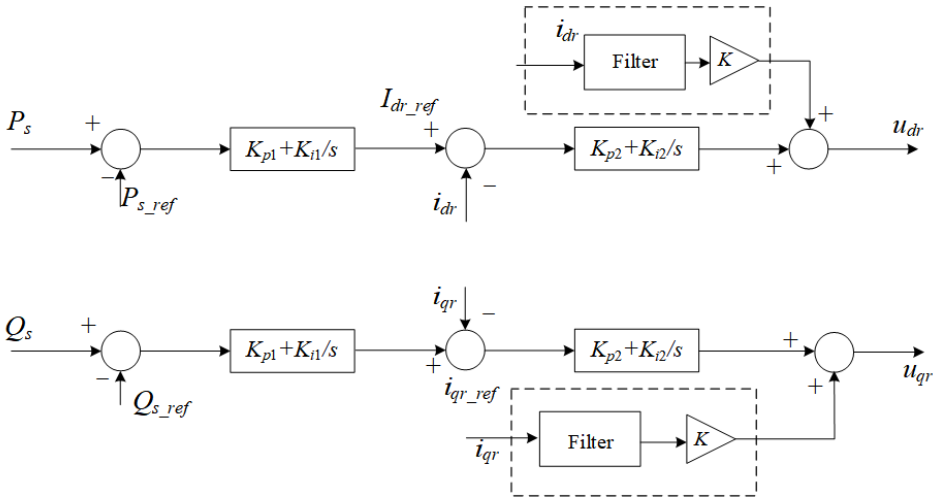

FIGURE 6. Virtual Resistance Controller

Using the rotor current as the two input signals of the virtual resistance controller, a virtual voltage is generated after filtering and proportional control Δu_r offsets the disturbance voltage caused by RSC controller parameters at sub-synchronous frequencies.

5. **Analysis of the mechanism of sub-synchronous oscillation and simulation verification of suppression measures.**

5.1. **Analysis and verification of the mechanism of sub-synchronous oscillation.**

In order to verify the correctness of the analysis theory of sub-synchronous oscillation caused by the grid connected system, the model was built in PSCAD/EMTDC, and the various parameter settings were consistent with the previously set parameters for sub-synchronous oscillation analysis. When the output power of the wind turbine decreases from 1 p.u. to 0.8 p.u. due to external interference, analyzing the distribution of eigenvalues on complex coordinates can directly determine the stability of the grid connected system. As shown in Figure 7, in the distribution of eigenvalues, there is a pair of conjugate complex roots located in the right half plane of the coordinate imaginary axis. As the output power of the wind farm decreases, there is an amplification oscillation of the system, and the damping of the system is -0.2099.

The following Figure 8 shows the wind farm output power graph when the wind farm output power decreases from 1 p.u. to 0.8 p.u. The system operates to a stable point and after being disturbed, the output power decreases. Due to the power decrease, the

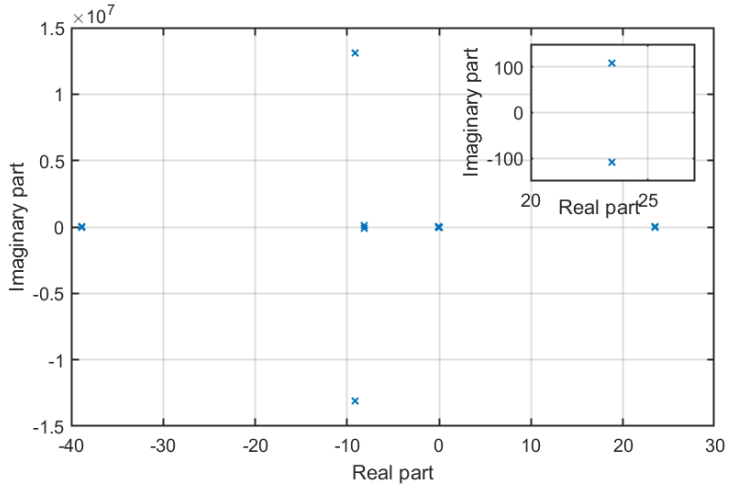

FIGURE 7. Distribution of Eigenvalues After Small Disturbances in Grid Connected Systems

system is located near the resonance point, resulting in an equal amplitude oscillation of the output power.

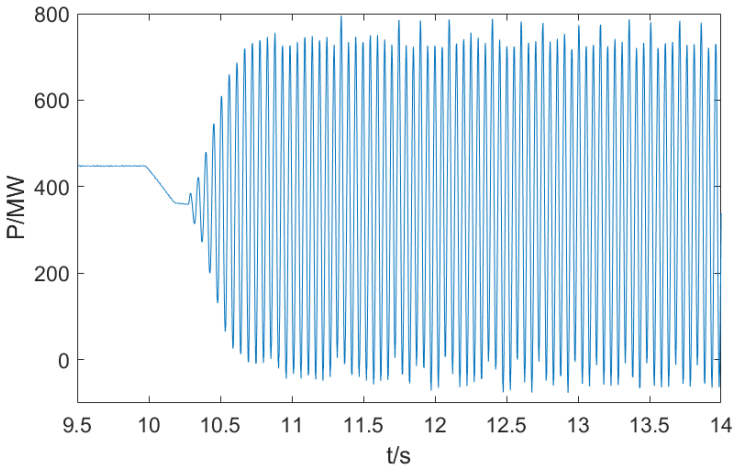

FIGURE 8. Wind Farm Side Output Power

Perform FFT (Fast Fourier transform) analysis on the output power of the wind farm, as shown in Figure 9. The frequency changes between 15Hz and 20Hz, reaching its maximum amplitude at f_m=19.82Hz, which is approximate in the above analysis values.

The following Figure 10 shows the voltage waveform of the busbar at the outlet of the wind farm, as shown in the figure. The voltage waveform exhibits oscillation phenomenon.

After FFT analysis of the bus voltage at the wind farm outlet, except for the power frequency of 50Hz, there is a non power frequency component with a frequency of 30.17Hz. The sum of this frequency and the output power frequency at the wind farm outlet is 50Hz, which is exactly complementary. Compared to the frequency close to 70Hz, the super synchronous component accounts for a larger proportion, as shown in Figure 11.

The above conclusion proves that the grid connected system has experienced sub-synchronous oscillation with a frequency of 19.82Hz, accompanied by the occurrence of supersynchronous oscillation.

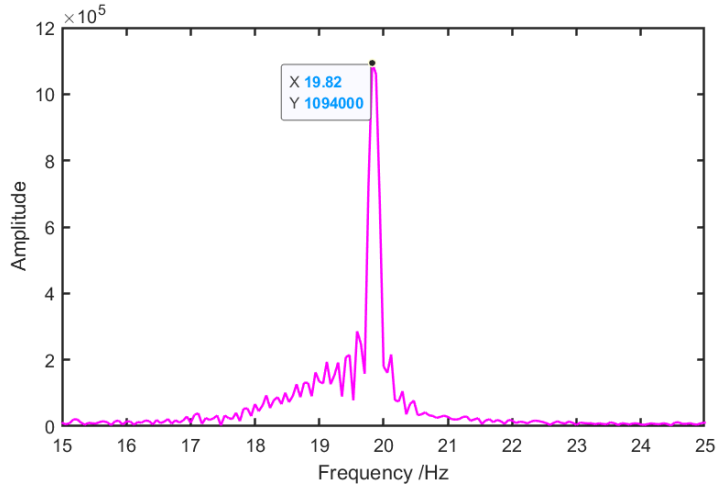

FIGURE 9. Wind Farm Side Output Power

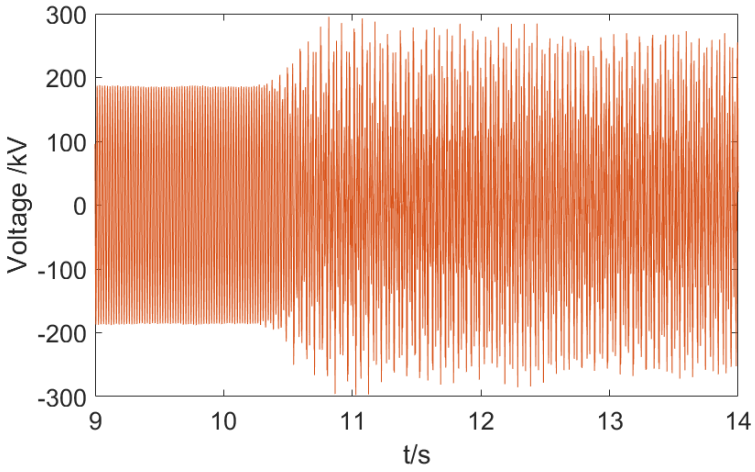

FIGURE 10. Voltage of the Busbar on the Outlet Side of the Wind Farm

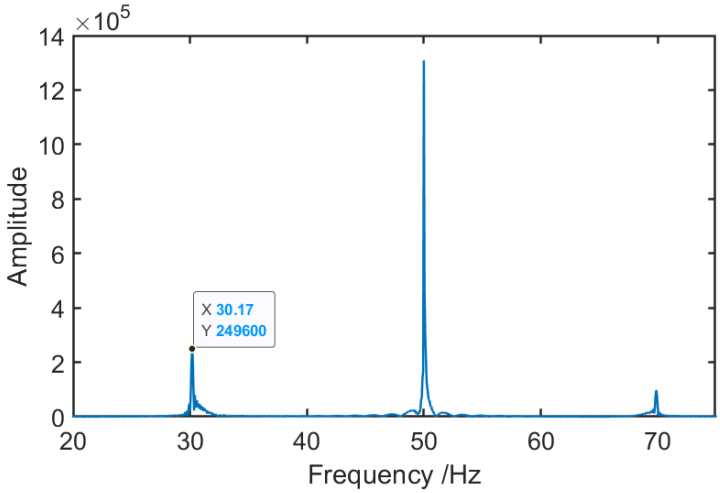

FIGURE 11. FFT Analysis of Bus Voltage on the Exit Side of the Wind Farm

5.2. **Simulation and verification of suppression strategies.** In order to verify the correctness of the mechanism analysis and control strategy in this article, the operating condition is set as the wind farm output power changes from 1 p.u. to 8 p.u.. Firstly, only control the DC component in the circulation, adjust k_{p8} and k_{i8} multiple times, and set other parameters as stable operating points.

As shown in Figure 12, the trajectory of the system's eigenvalues can be obtained. The eigenvalues show a turning point when approaching the real axis, and the system is still in a negative damping state. Under the operating conditions of the system, controlling only the DC component in the circulating current is not sufficient to change the negative damping state of the system. Therefore, it is necessary to consider collaborating the DC component control with the virtual resistance controller.

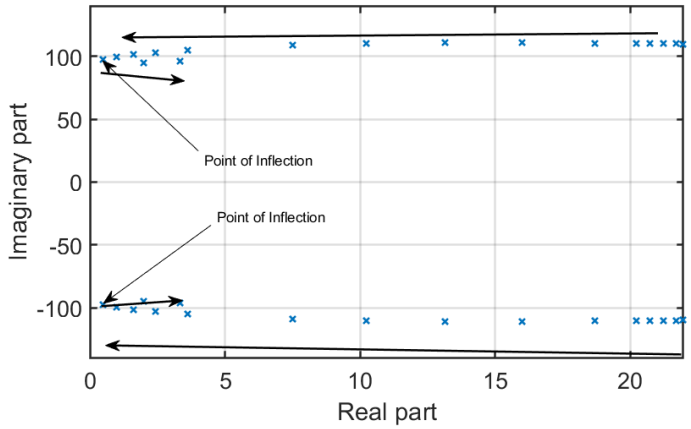

FIGURE 12. Trajectory of Eigenvalue Changes when Suppressing Only the DC Component

Add a virtual resistance controller and set the values of k_{p8} and k_{i8} at the inflection point unchanged. According to the initial value of K set above, the fixed value of RRSC follows the fixed values of k_{p1}, k_{p2}, k_{i1} and k_{i2}. By changing the fixed values of the four parameters, continuous control of the virtual resistance value R_{RSC} is achieved. By continuously adjusting the fixed values, the result is shown in Figure 13, The collaborative control strategy of adding virtual resistors continuously moves the distribution of eigenvalues towards the left half plane of the coordinates, and the imaginary part value decreases continuously, resulting in a decrease in oscillation frequency. The synergy of the two control strategies effectively changes the negative damping state of the system and improves the overall damping level of the system.

Further verification of the effectiveness of the suppression measures is shown in Figure 14, which shows the power output of the wind farm at the outlet side. At 7 seconds, the output power of the wind farm decreased from 1 p.u. to 0.8 p.u., and the output power of the wind farm oscillated with equal amplitude. After adding the suppression measures around 11.5 seconds, the output power of the wind farm remained stable at 8 p.u.

The three-phase voltage on the outlet side of the wind farm is shown in Figure 15, and there is also an equal amplitude oscillation. However, after applying suppression measures, the amplitude of the three-phase voltage remains at the level before the oscillation. FFT analysis of the suppressed voltage waveform is shown in Figure 16.

As shown in Figure 16, there are no frequencies on other components except for the power frequency component, indicating that adding a virtual resistor controller on top of

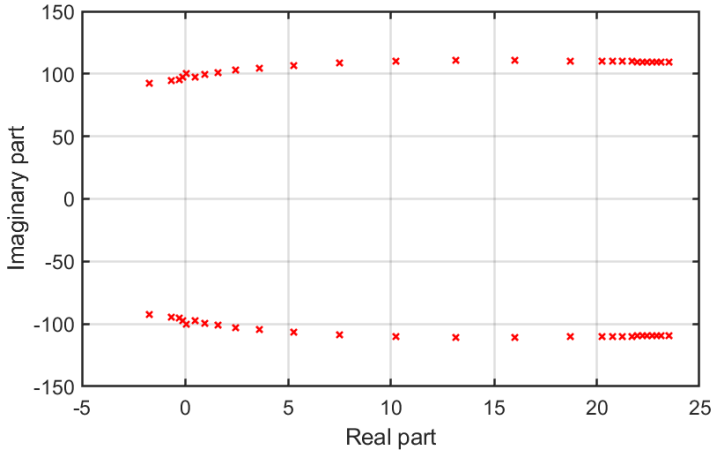

FIGURE 13. Characteristic Value Variation Trajectory of DC Component Controlled Collaborative Virtual Resistance Controller

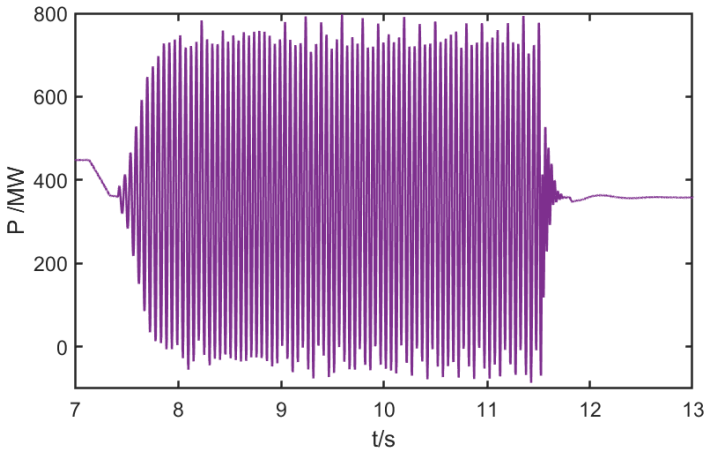

FIGURE 14. Wind Farm Output Power

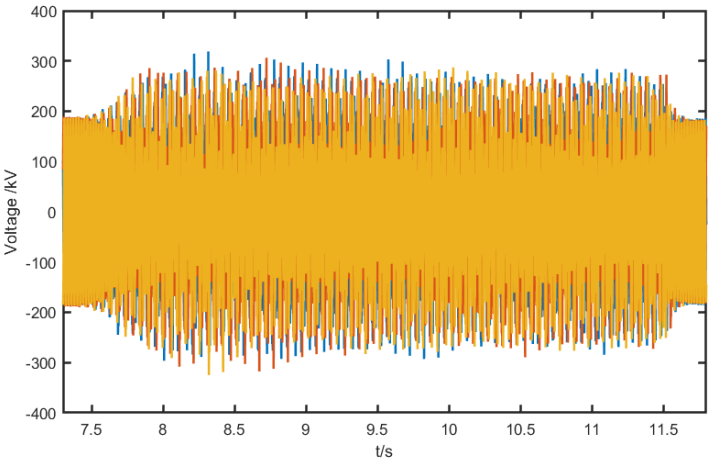

FIGURE 15. Three Phase Voltage at the Outlet Side of the Wind Farm

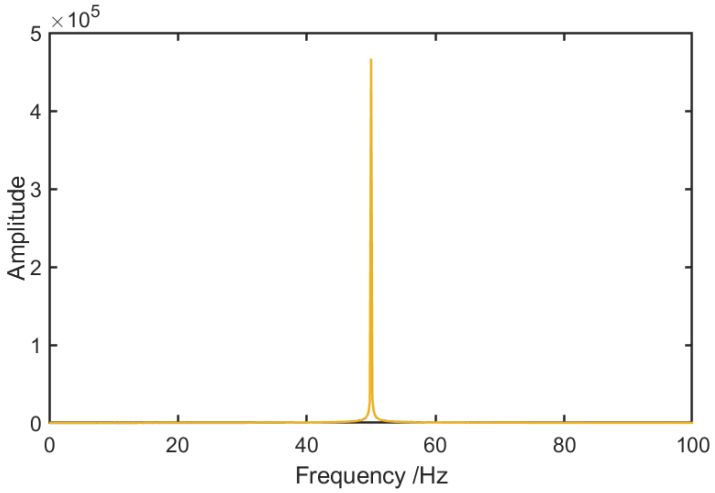

FIGURE 16. FFT Analysis Spectrum of Three-phase Voltage at the Outlet Side of the Wind Farm

the original DC component control effectively suppresses the problem of sub-synchronous oscillation in the grid connected system.

6. **Conclusion.** This paper explores various types of sub-synchronous oscillations that are generated by offshore doubly-fed wind turbines connected to the power grid through MMC-HVDC. The analysis leads to two distinct types of subsynchronization: disturbance current reacting to DFIG-PWM grid side controller causing SSEI, and power fluctuation in MMC-HVDC control side causing SSTI. The study also proposes an improved suppression strategy using a DC control with circulation suppressor and virtual resistance controller. The efficacy of this strategy is validated by PSCAD/EMTDC simulation.

REFERENCES

[1] Y.-F. Xi, C. Tang , Y.-H. Huang, D. Wang, M. Yi, B.-Y Xiong, "Dominant mode and participation factor analysis of sub-synchronous oscillation of wind power connected to weak transmission end of the flexible HVDC system," *Power System Automation*, vol. 42, no. 17, pp. 25-33, 2018.

[2] Y.-F. Wang, C.-Y. Zhao, C.-Y. Guo, "Small signal stability analysis and oscillation suppression method for DC transmission grid connected system with modular multi-level converters in doubly fed wind farms," *Journal of Electrical Engineering*, vol. 34, no. 10, pp. 2116-2129, 2019.

[3] X.-Y. Bian, Y. Ding, K. Mai, Q.-B. Zhou, Y. Zhao, L.-J. Tang., "Subsynchronous oscillation caused by grid-connection of offshore wind farm through VSC-HVDC and its mitigation," *Automation of Electric Power Systems*, vol. 42, no. 17, pp. 25-33, 2018.

[4] C. Lv, N.-L. Tai., "Control for offshore wind power integration based on modular multilevel converter," *The Journal of Engineering*, vol. 2017, no. 13, pp. 1885-1889, 2017.

[5] K. Sun, W. Zhao, J.-Y. Wen, "Mechanism and characteristics analysis of subsynchronous oscillation caused by DFIG-based wind farm integrated into grid through VSC-HVDC system," *Proceedings of the CSEE*, vol. 38, no. 22, pp. 6520-6533, 2018.

[6] X. Yu, W.-H. Chen., "Review of subsynchronous oscellation induced by wind power generation integrated system," *Power Generation Technology*, vol. 39, no. 4, pp. 304-312, 2018.

[7] W. Hua, W. Dong, L. Ye, S.-X. Li, Z.-R. Zhang, Z. Xu., "Study on transient synchronous stability of PLL-GFC MMC-HVDC," *Zhejiang Electric Power*, vol. 42, no. 1, pp. 13-22, 2023.

[8] B. Zhou, J.-N. Xu., "Research on a harmonic injection modulation strategy to optimize the operating characteristics of MMC-HVDC," *Electrical Technology*, vol. 23, no. 5, pp. 5-15, 2022.

[9] X.-Y. Hao, C.-Y. Guo, W. Jiang, M.-L. Peng, X. Lin, "Identification method equivalent impedance of AC power grid connected to MMC-HVDC system based on reactive power injection," *Automation of Electric Power Systems*, vol. 47, no. 9, pp. 184-192, 2023.

[10] T. Liang, Z.-G. Hou, J.-H. Zou, Y.-J. Zhang., "Design and application of SCADA system for wind farms based on cloud computing platform," *Chinese High Technology Letters*, vol. 28, no. 1, pp. 8-14, 2018.

[11] T.-Y. Wu, F. Kong, Q. Meng, S. Kumari, and C.-M. Chen, "Rotating behind security: an enhanced authentication protocol for iot-enabled devices in distributed cloud computing architecture," *EURASIP Journal on Wireless Communications and Networking*, vol. 2023, 36, 2023.

[12] Y.-G. Li, W.-C. Chu, H.-Z. Liu, "Low-frequency oscillation characteristic analysis of grid-connected VSG-PMSG via MMC-HVDC system," *Electric Power Automation Equipment*, vol. 1, no. 1, pp. 1-14, 2023.

[13] T.-Y. Wu, L. Wang, X. Guo, Y.-C. Chen, and S.-C. Chu, "Sakap: Sgx-based authentication key agreement protocol in iot-enabled cloud computing," *Sustainability*, vol. 14, 11054, 2022.

[14] C.-M. Chen, Z. Tie, E. K. Wang, M. K. Khan, S. Kumar, and S. Kumari, "Verifiable dynamic ranked search with forward privacy over encrypted cloud data," *Peer-to-Peer Networking and Applications*, vol. 14, no. 5, pp. 2977–2991, 2021.

[15] J. Liu, W. Yao, J.-Y. Wen., "Small signal stability analysis and control of double-fed induction generator considering influence of PLL and power grid strength," *Proceedings of the CSEE*, vol. 37, no. 11, pp. 3162-3173, 2017.

[16] Y. Wang, "Modeling and simulation of hybrid-HVDC system based on LCC and VSC," MA.Eng. dissertation, Shandong University of Science and Technology, 2018.

[17] H. Xiong, Z. Qu, X. Huang, and K.-H. Yeh, "Revocable and unbounded attribute-based encryption scheme with adaptive security for integrating digital twins in internet of things," *IEEE Journal on Selected Areas in Communications*, vol. 41, no. 10, pp. 3306–3317, 2023.

[18] L. Wang, Y. Lin, T. Yao, H. Xiong, and K. Liang, "Fabric: Fast and secure unbounded cross-system encrypted data sharing in cloud computing," *IEEE Transactions on Dependable and Secure Computing*, vol. 20, no. 6, pp. 5130–5142, 2023.

[19] B. M, L. E V, P. R J., "Experience with HVDC-turbine-generator torsional interaction at Square Butte," *IEEE Transactions on Power Apparatus and Systems*, vol. PAS-99, no. 3, pp. 966-975, 1980.

[20] Y.-J. Guan., "Research on sub-synchronous oscillation detection and suppressing technology for wind farms connected with transmission systems," MA.Eng. dissertation, Southeast University, 2019.